

Beam Energy Dependence of Rapidity-Even Dipolar Flow in Au+Au Collisions

Niseem Magdy^{1,*} and Roy A. Lacey^{1,†}

¹*Department of Chemistry, State University of New York,
Stony Brook, New York 11794, USA*

Abstract

Measurements for directed flow, characterized by the Fourier coefficient v_1 , are presented for a broad range of transverse momenta (p_T) and centrality intervals in Au+Au collisions ($\sqrt{s_{NN}} = 7.7 - 200$ GeV) recorded by the STAR experiment. The measurements validate the important influence of momentum conservation and the characteristic dependencies on $\sqrt{s_{NN}}$, centrality and p_T , expected when initial-state geometric fluctuations act in concert with hydrodynamic-like expansion to generate rapidity-even dipolar flow. The $\sqrt{s_{NN}}$, centrality and p_T dependencies of v_1 , as well as an observed similarity between its excitation function and that for v_3 , could serve as constraints for initial-state models, and for precision extractions of the temperature dependence of the specific shear viscosity.

* Niseem.Abdelrahman@stonybrook.edu

† Roy.Lacey@stonybrook.edu

CONTENTS

I. Data, Event and Track selection	3
II. Analysis Method	6
A. Correlation function technique	6
1. The $\Delta\eta$ effect	7
B. Comparison with the published results	15
C. Dipolar flow (v_1^{even}) and long rang non-flow subtraction	17
1. Extraction of dipolar flow (v_1^{even})	18
D. Cross-checks	22
E. Systematic uncertainty estimates	24
1. Systematic uncertainty estimates associated with the correlation function	24
2. Systematic uncertainty estimates associated with the v_{11} fit method	24
3. Systematic uncertainty from fitting procedure	25
F. Fit χ^2	25
III. Paper Results	31
References	34

I. DATA, EVENT AND TRACK SELECTION

The data and the associated cuts (vertex cut, trigger-ID, nHitMin, DCA, p_T , η , etc) used in the analysis are summarized in Tables I and II. Tables I summarizes the Trigger, Production, Trigger ID and and vertex cut respectively. The centrality selections are based on StRefMultCorr Class from:*offline/users/hmasui/StRefMultCorr*.

The track cuts are summarized in Table II. More information about (QA, bad runs) could be found in this link,

http://www.star.bnl.gov/protected/heavy/aschmah/Presentations/LFS_RefMult_QA_100711_V1.pdf

Trigger Name	Production	Vertex Cut	Trigger ID
<i>AuAu7 – Production</i>	<i>P10ih</i>	$ V_z < 70cm $	290001
			290003
			290004
<i>AuAu11.5 – Production</i>	<i>P10ih</i>	$ V_z < 50cm $	310013
			310014
<i>AuAu14.5 – Production</i>	<i>P14ii</i>	$ V_z < 40cm $	440005
			440015
<i>AuAu19.6 – Production</i>	<i>P11id</i>	$ V_z < 40cm $	340001
			340002
			340011
			340012
			340021
			340022
<i>AuAu27 – Production</i>	<i>P11id</i>	$ V_z < 40cm $	360001
			360002
<i>AuAu39 – Production</i>	<i>P10ih</i>	$ V_z < 40cm $	380001
			380002
<i>AuAu62.4 – Production</i>	2004	$ V_z < 30cm $	270001
			270005
			270011
			270021
<i>AuAu200 – Production</i>	2004	$ V_z < 30cm $	15007

Tab. I. Summary of the selections for Trigger, production, vertex cut and trigger ID.

Cut	$TPC - tracks$
$DCA\ cm$	< 3
$p_T\ GeV/c$	> 0.2
$ \eta \ cm$	< 1
$nHitMin$	> 10
V_r	< 2

Tab. II. The track cuts employed in the analysis .

II. ANALYSIS METHOD

This analysis follows two major steps. In the first step, a correlation function technique is used to extract v_{nn} . In the second, the extracted values of v_{nn} are used in concert with a simultaneous fitting procedure to extract v_1^{even} . In the following, both steps are summarized.

A. Correlation function technique

All techniques used to extract v_n are related to the correlation function. The correlation function carry flow and non-flow(HBT, Resonance decay and Jet like correlations) signals as well as some residual detector effects(track merging/splitting). The correlation function technique allows straightforward extraction of v_{nn} with the possibility to suppress non-flow and residual detector effects.

The two particle azimuthal correlation function $C(\Delta\phi, \Delta\eta)$ can be expressed as,

$$C(\Delta\phi, \Delta\eta) = \frac{(dN/d\Delta\phi)_{Same}}{(dN/d\Delta\phi)_{Mix}} \quad (1)$$

where $(dN/d\Delta\phi)_{Same}$ is the distribution of charged hadron pairs from the *same* event and $(dN/d\Delta\phi)_{Mix}$ is the pair distribution for particles selected from different events, belonging to the same class; $\Delta\phi$ is the azimuthal angle difference for particle pairs. Event classes, which retain the residual detector single particle relative efficiencies etc., eliminate the the genuine two-particle physics correlations. To optimize mixing, events are pooled into classes to ensure similar global characteristics for same-event and mixed-event tracks. Twenty Vz classes and 10 centrality classes were used. A pool depth of 10 was employed for mixing.

The Fourier coefficients v_{nn} , used to characterize the magnitude of the azimuthal anisotropy, are obtained from the correlation function as,

$$v_{nn} = \frac{\sum_{\Delta\phi} C(\Delta\phi, \Delta\eta) \cos(n\Delta\phi)}{\sum_{\Delta\phi} C(\Delta\phi, \Delta\eta)}, \quad (2)$$

where $C(\Delta\phi, \Delta\eta) = \frac{(dN/d\Delta\phi)_{Same}}{(dN/d\Delta\phi)_{Mix}}$. For flow dominated correlations, the Fourier coefficient v_{nn} factorizes into the product of two single-particle distributions:

$$v_{nn}(p_T^b, p_T^a) = v_n(p_T^b) v_n(p_T^a), \quad (3)$$

For a fixed- p_T selection

$$v_{nn} = \frac{\sum_{\Delta\phi} C(\Delta\phi, \Delta\eta) \cos(n\Delta\phi)}{\sum_{\Delta\phi} C(\Delta\phi, \Delta\eta)}. \quad (4)$$

The two particle correlation functions from which v_{nn} is extracted, could have both flow and non-flow correlations. The short range non-flow can be suppressed with a $\Delta\eta$ cut, as discussed below.

1. The $\Delta\eta$ effect

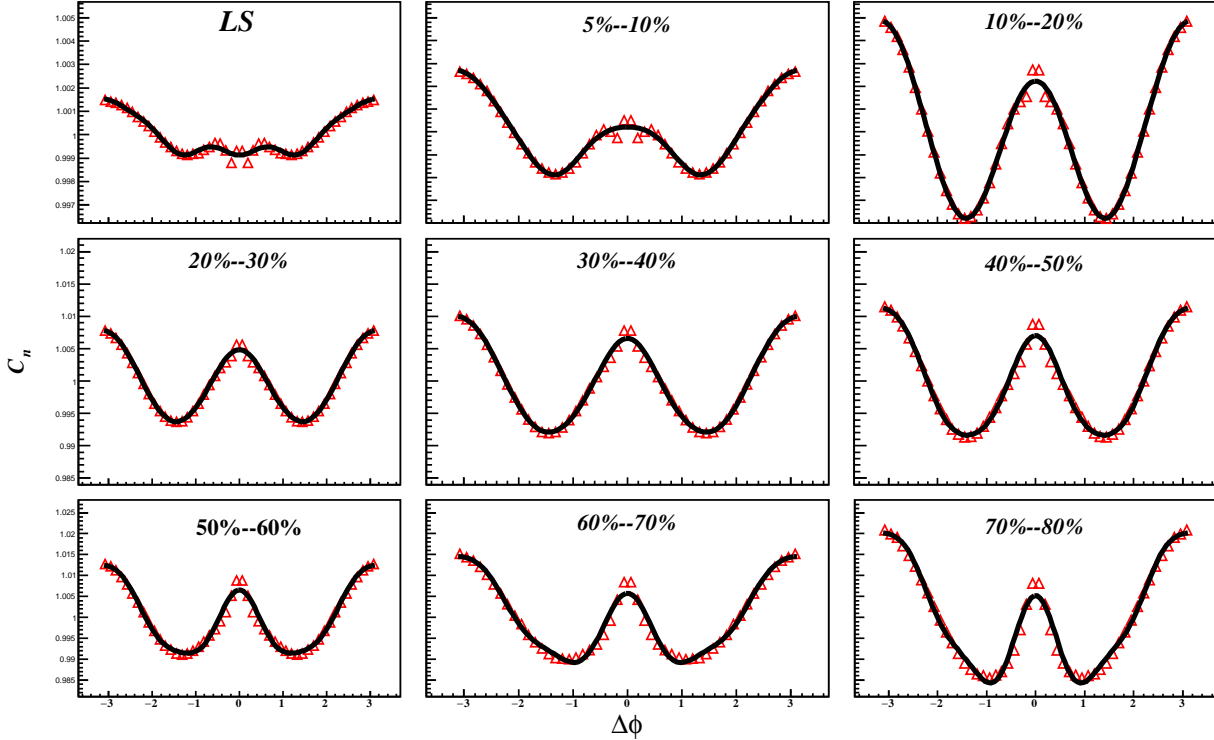


Fig. 1. Like sign (LS) p_T -integrated correlation function for Au+Au collisions at $\sqrt{s_{NN}} = 39$ GeV. The correlation functions are generated without a $\Delta\eta$ cut.

Representative examples of the correlation functions obtained in this analysis are shown in Figs. 1, 2 and 3 for several centrality selections and beam energies. These correlation functions reflect both flow and non-flow contributions, as well as some residual detector/tracking effects.

The latter effects are especially evident in the top left panels of Figs. 1 and 2 where a dip and a peak in the correlation function at $\Delta\phi \sim 0$ is evident. We attribute the dip (peak) to track merging (splitting) effects. The short-range non-flow contributions (HBT, Resonance decay and Jet-like correlations) and the residual detector effects (track merging/splitting)

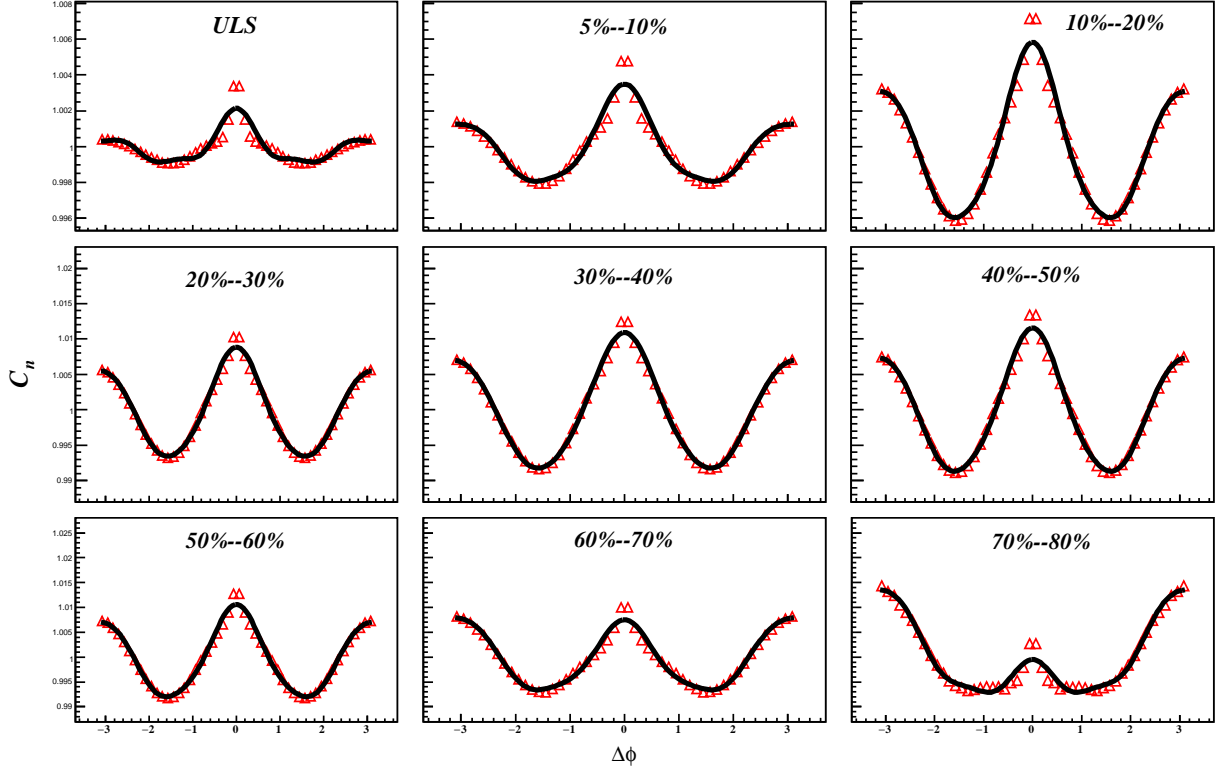


Fig. 2. Unlike sign (ULS) p_T -integrated correlation functions for Au+Au collisions at $\sqrt{s_{NN}} = 39$ GeV for several centrality selections. The correlation functions are generated without a $\Delta\eta$ cut.

dominate at small $\Delta\eta$. Consequently, we explored the utility of a $|\Delta\eta|$ cut to suppress these effects.

The correlation functions shown in Figs. 1 and 2 were generated for the full $\Delta\eta$ range for both like sign (LS) and unlike sign (ULS) charged hadrons. They indicate that the distortions which result from non-flow contributions and detector effects, persist over the full range of centralities. Similar results were obtained for other beam energies.

To suppress these distortions, the correlation functions were studied as a function of $\Delta\eta$ cut, for several p_T and centrality selections, over the full span of beam energies. This comprehensive study indicated that the cut $|\Delta\eta| > 0.7$, leads to significant suppression of track merging/splitting and non-flow contributions, while allowing reasonable statistical significance for our study over the full beam energy range. Here, it is noteworthy that a large $|\Delta\eta|$ leads to a significant reduction in the available statistics, especially for the lower

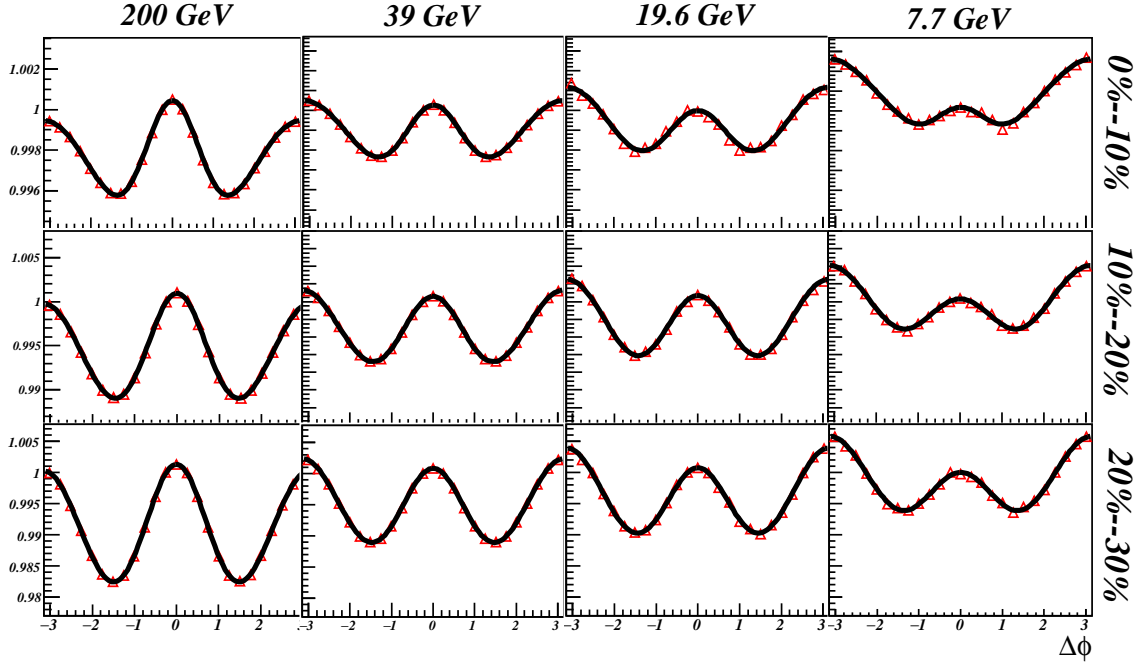


Fig. 3. p_T -integrated correlation functions for Au+Au collisions for several centralities and beam energies as indicated; the correlation functions are generated for $|\Delta\eta| > 0.7$.

beam energies.

The representative set of correlation functions shown in Fig. 3, clearly indicates that the “distortions” [due to detector effects and non-flow] evident in Figs. 1 and 2 are suppressed by the $|\Delta\eta| > 0.7$ cut.

A further study, involving LS and ULS charged hadrons was employed to validate the effectiveness of the $|\Delta\eta|$ cut for suppressing short-range non-flow contributions and to estimate their influence on the magnitude of the extracted values of v_n .

Here, the essential idea is that the LS and ULS selections can be used to enhance the respective short-range contributions due to HBT, Resonance decay, Jet-like correlation, etc. We use the similarity between the v_n values extracted from LS and ULS correlation functions as a figure of merit for the suppression of short-range non-flow contributions.

For each beam energy, correlation functions were generated for several $|\Delta\eta|$ selections for both LS and ULS charged hadrons. The resulting correlation functions were then Fourier analyzed (cf. Eqs. 2 and 3) to obtain $v_n(\text{cent})$ for further comparisons. Representative

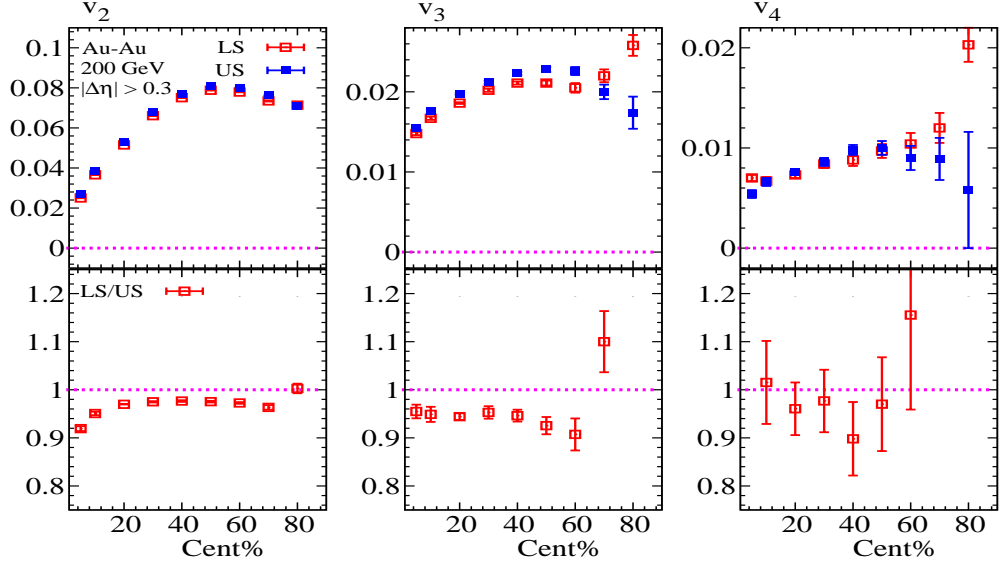


Fig. 4. Comparison of LS- and ULS- v_n ($n > 1$) for Au+Au collisions at $\sqrt{s_{NN}} = 200$ GeV for $|\Delta\eta| > 0.3$.

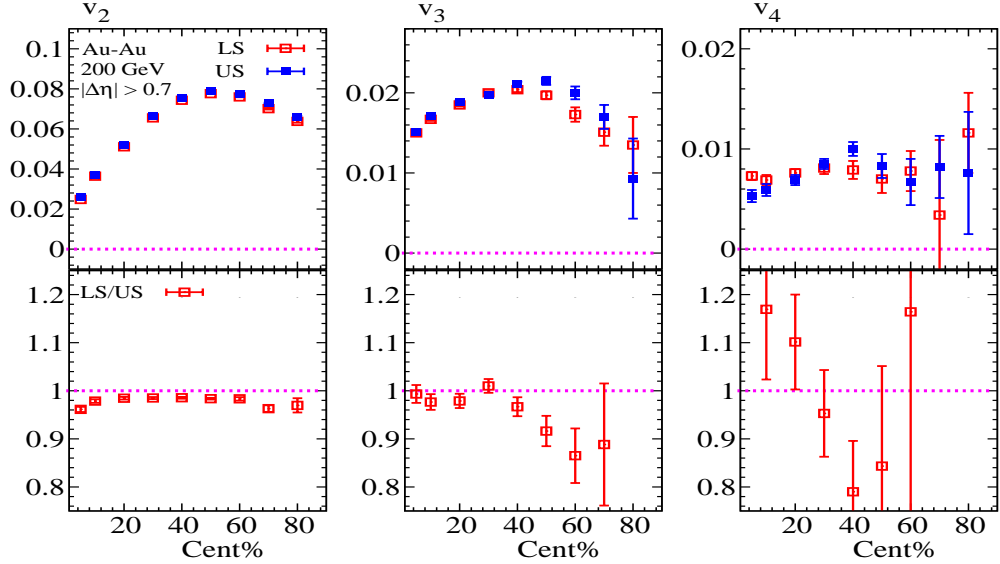


Fig. 5. Comparison of LS- and ULS- v_n for ($n > 1$) for Au+Au collisions at $\sqrt{s_{NN}} = 200$ GeV for $|\Delta\eta| > 0.7$.

results from this study are shown for Au+Au collisions at $\sqrt{s_{NN}} = 200, 39$, and 11.5 GeV (respectively) in Figs. 4 - 12. The bottom panels in these figures give the ratio (LS/US) of the v_n values shown in the top panels.

The comparisons shown in Figs. 4, 7 and 10 for LS- and ULS- v_n for $|\Delta\eta| > 0.3$, indicate

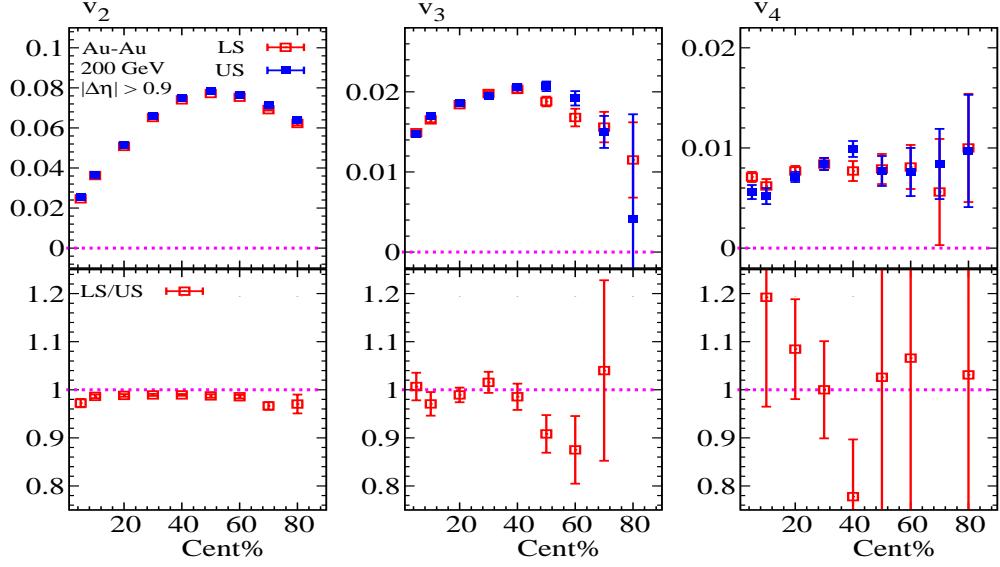


Fig. 6. Comparison of LS- and ULS- v_n ($n > 1$) for Au+Au collisions at $\sqrt{s_{NN}} = 200$ GeV for $|\Delta\eta| > 0.9$.

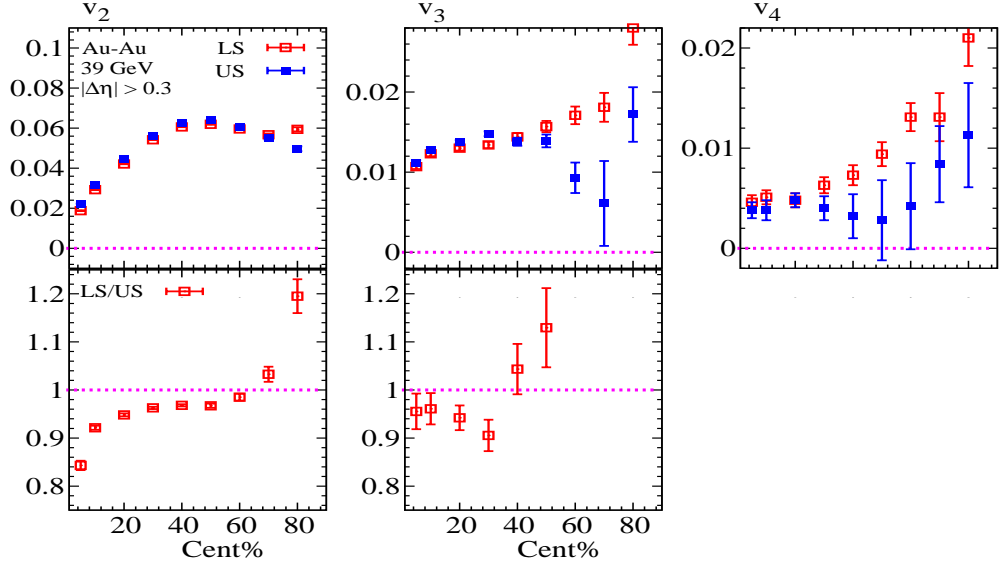


Fig. 7. Comparison of LS- and ULS- v_n ($n > 1$) for Au+Au collisions at $\sqrt{s_{NN}} = 39$ GeV for $|\Delta\eta| > 0.3$.

clear differences which vary with centrality and $\sqrt{s_{NN}}$. We attribute these differences to the influence of short-range non-flow contributions. Figs. 5, 8 and 11 show that these differences are significantly reduced for $|\Delta\eta| > 0.7$, confirming the utility of this cut for suppressing non-flow contributions. Figs. 6, 9 and 12 indicate that a further increase to $|\Delta\eta| > 0.9$

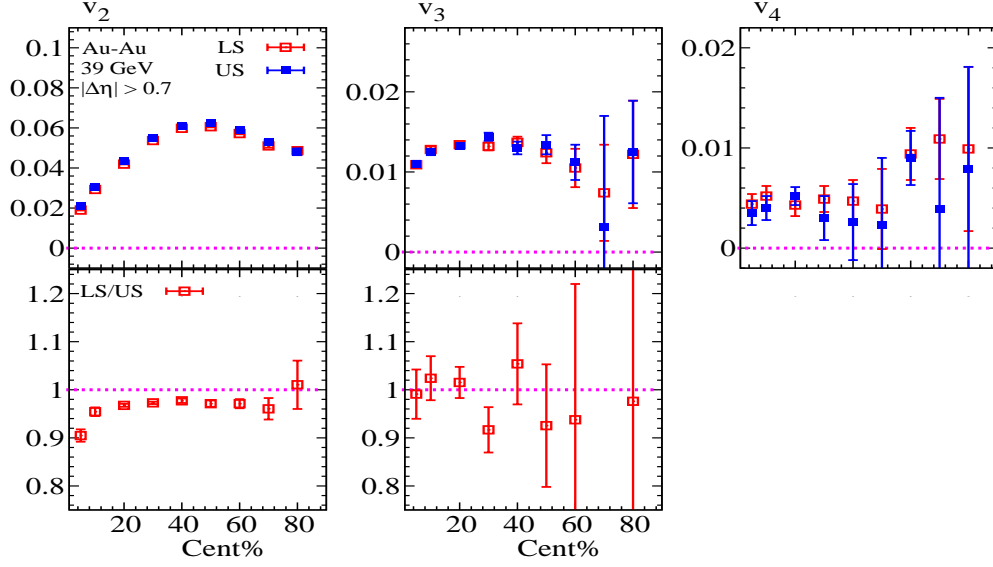


Fig. 8. Comparison of LS- and ULS- v_n ($n > 1$) for Au+Au collisions at $\sqrt{s_{NN}} = 39$ GeV for $|\Delta\eta| > 0.7$.

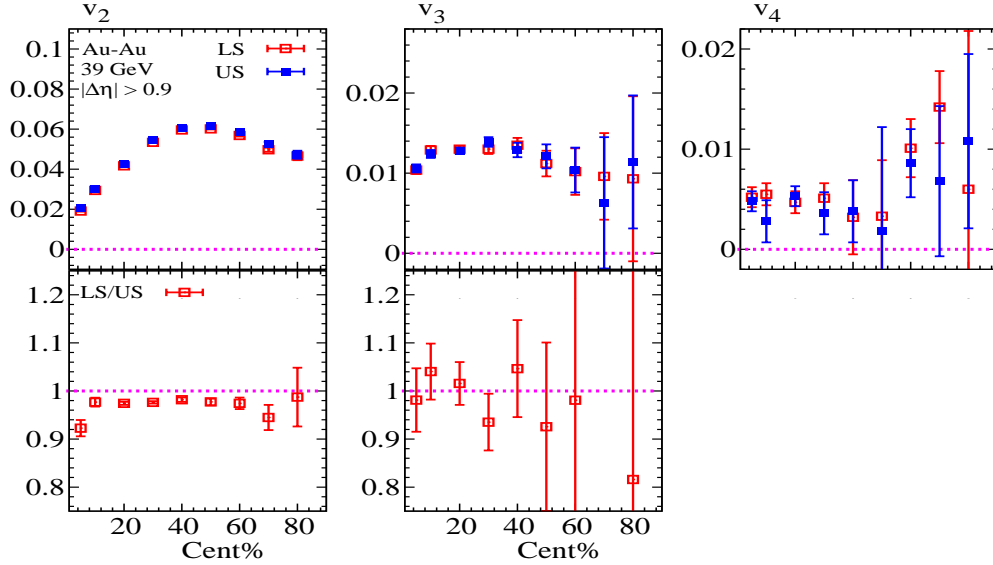


Fig. 9. Comparison of LS- and ULS- v_n ($n > 1$) for Au+Au collisions at $\sqrt{s_{NN}} = 39$ GeV for $|\Delta\eta| > 0.9$.

leads to little, if any, improvement in the agreement between the LS- and ULS- v_n values. However, one can see a clear deterioration in the statistical significance of the measured v_n values, especially for the higher harmonics. Consequently, the cut $|\Delta\eta| > 0.7$, was employed to suppress short-range non-flow contributions for the full span of beam energies studied.

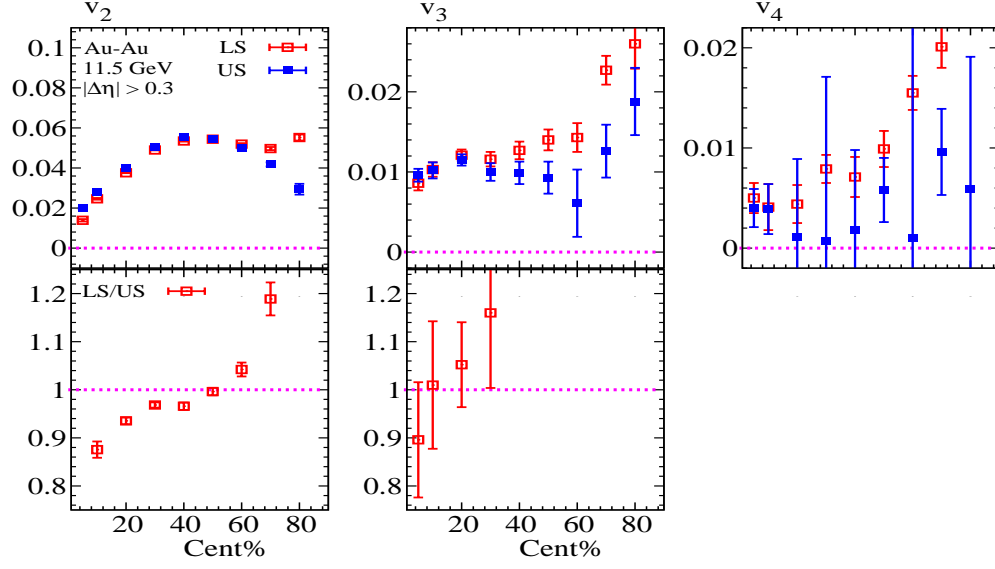


Fig. 10. Comparison of LS- and ULS- v_n ($n > 1$) for Au+Au collisions at $\sqrt{s_{NN}} = 11.5$ GeV for $|\Delta\eta| > 0.3$.

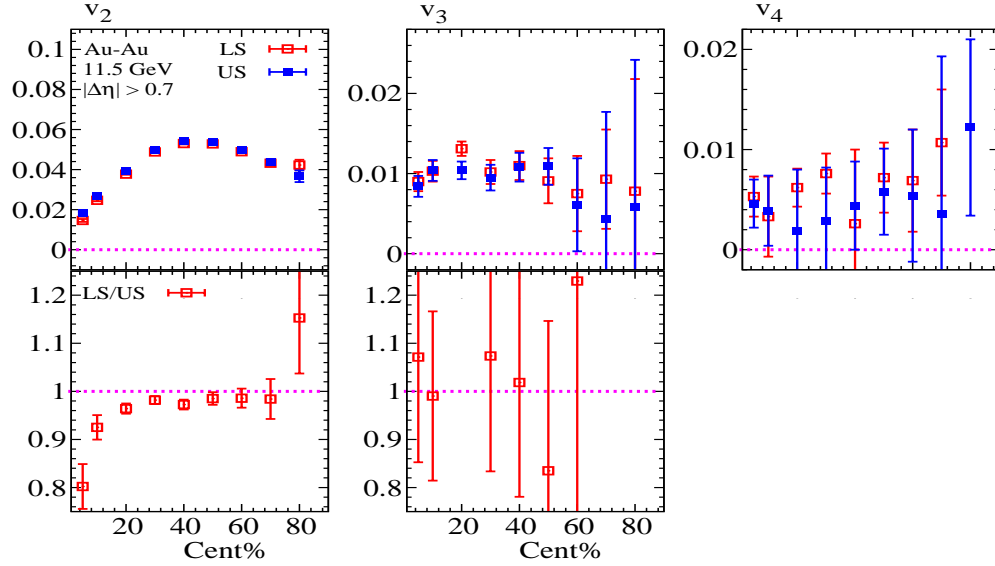


Fig. 11. Comparison of LS- and ULS- v_n ($n > 1$) for Au+Au collisions at $\sqrt{s_{NN}} = 11.5$ GeV for $|\Delta\eta| > 0.7$.

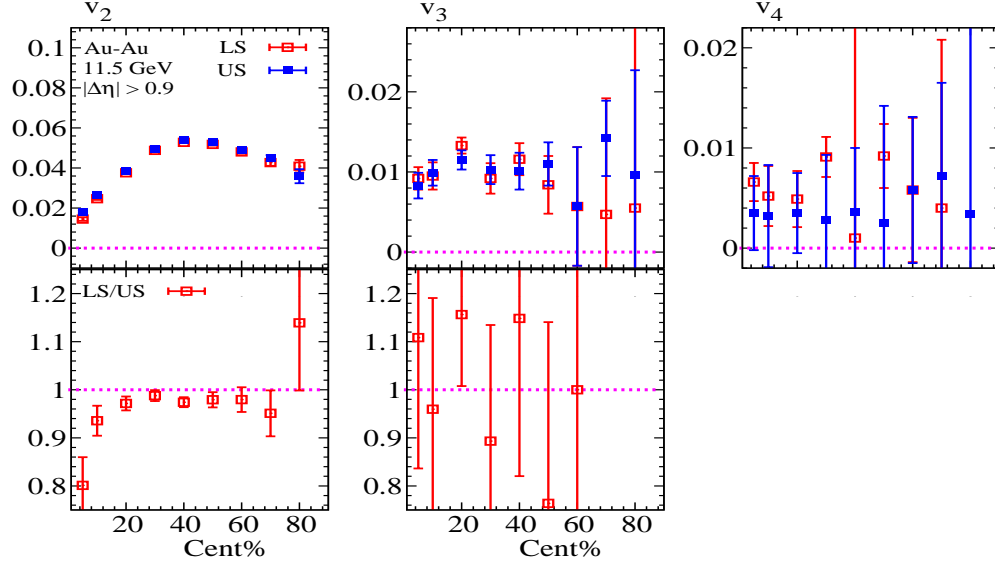


Fig. 12. Comparison of LS- and ULS- v_n ($n > 1$) for Au+Au collisions at $\sqrt{s_{NN}} = 11.5$ GeV for $|\Delta\eta| > 0.9$.

B. Comparison with the published results

Here we will compare our v_3 with the published one.

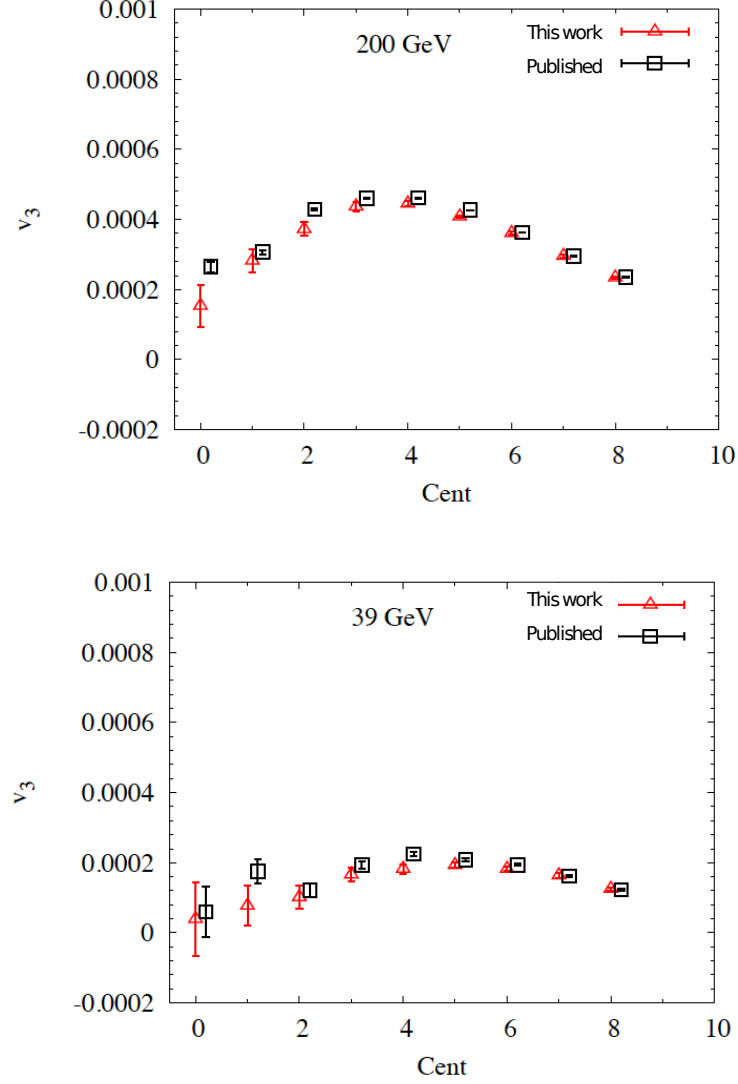


Fig. 13. The v_3 extracted from our correlation function compared to the published one at different beam energies.

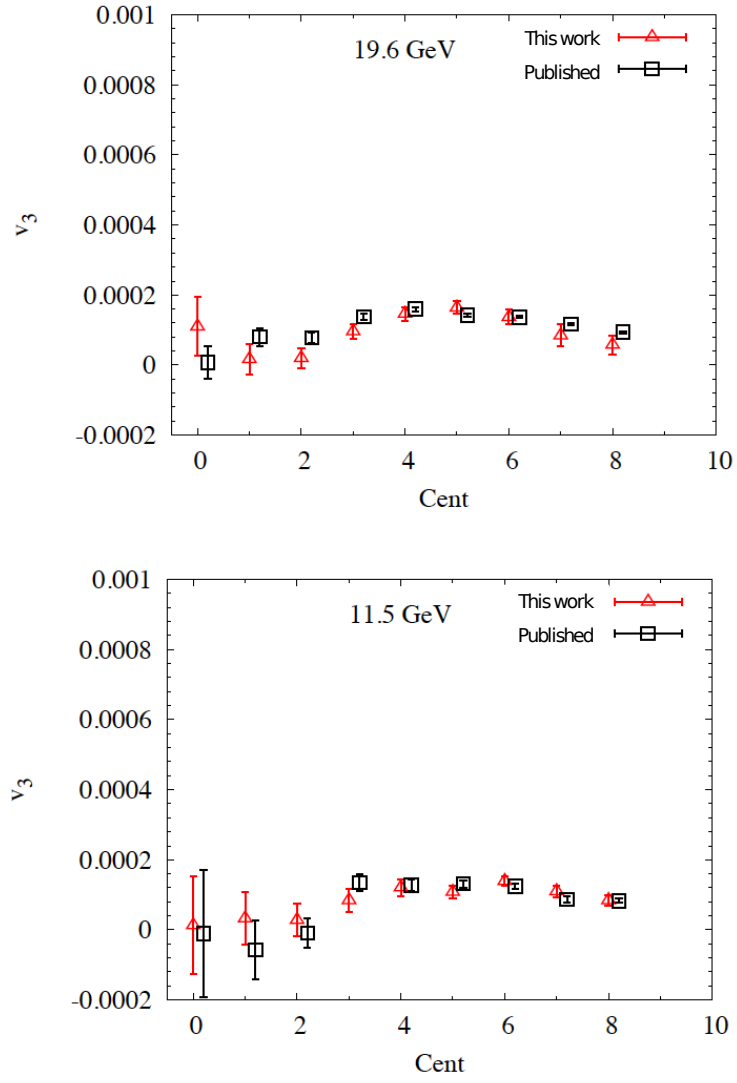


Fig. 14. The v_3 extracted from our correlation function compared to the published one at different beam energies.

C. Dipolar flow (v_1^{even}) and long rang non-flow subtraction

As discussed earlier, the two particle Fourier coefficient v_{nn} are obtained from the correlation function Fig.(3) as,

$$v_{nn} = \frac{\sum_{\Delta\phi} C(\Delta\phi, \Delta\eta) \cos(n\Delta\phi)}{\sum_{\Delta\phi} C(\Delta\phi, \Delta\eta)}, \quad (5)$$

where $C(\Delta\phi, \Delta\eta) = \frac{(dN/d\Delta\phi)_{\text{Same}}}{(dN/d\Delta\phi)_{\text{Mix}}}$.

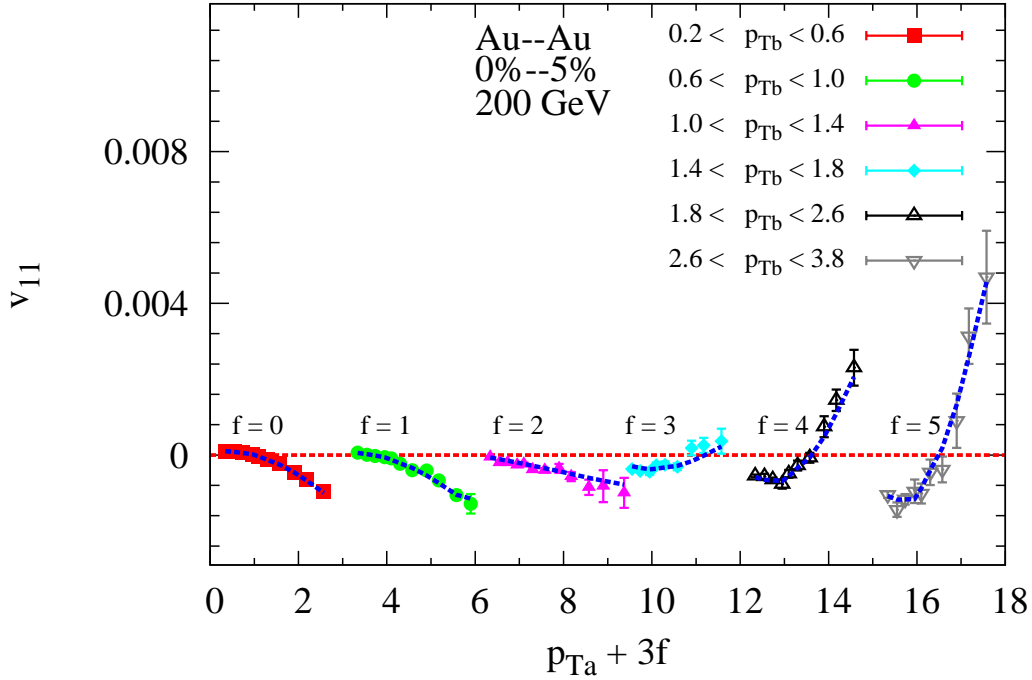


Fig. 15. Illustration of the simultaneous fit of $v_{1,1}$ Au+Au data ($\sqrt{s_{NN}} = 200$ GeV) with Eq. 7.

The Fourier coefficients v_{nn} factorizes into the product of two single-particle distributions:

$$v_{nn}(p_T^b, p_T^a) = v_n(p_T^b) v_n(p_T^a), \quad (6)$$

where the superscripts a and b refer to 2-particles that can be taken from different p_T bins. Several studies (including this work) have shown that, while this factorization holds reasonably well for $n > 1$ evaluated with a sizable $\Delta\eta$ gap, it breaks down for $n = 1$.

This break down is to be expected for v_1 due to the strong influence of long-range correlations induced by global momentum conservation. Since such correlations add to the flow

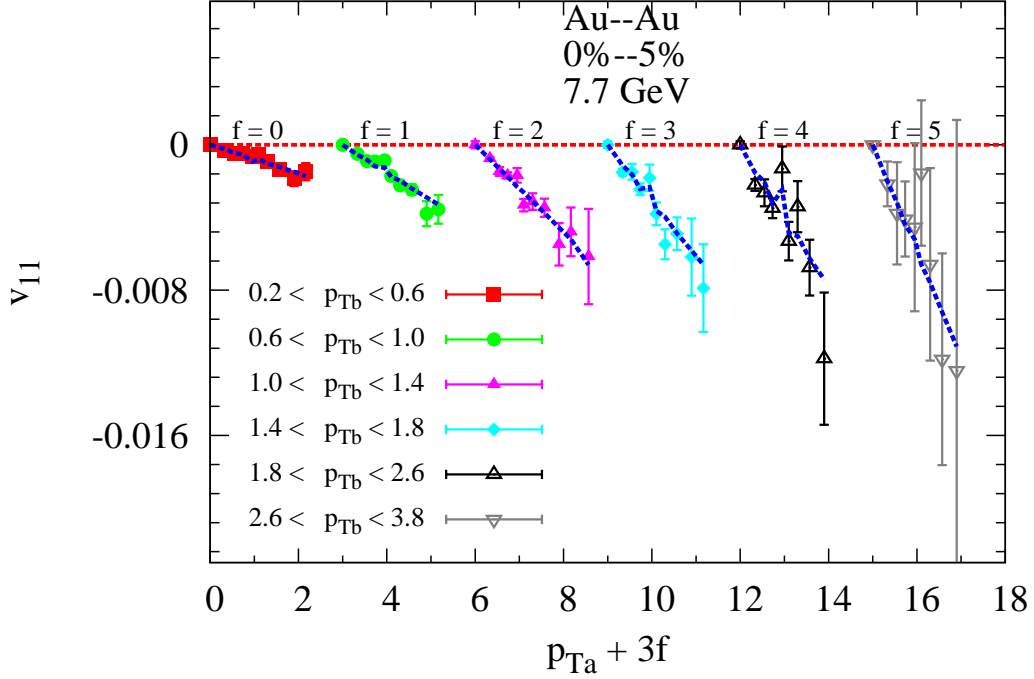


Fig. 16. Illustration of the simultaneous fit of $v_{1,1}$ Au+Au data ($\sqrt{s_{NN}} = 7.7$ GeV) with Eq. 7.

correlations of interest, it is necessary to subtract them;

$$v_{1,1}(p_T^b, p_T^a) = v_1(p_T^b)v_1(p_T^a) - \frac{p_T^b p_T^a}{M \langle p_T^2 \rangle}, \quad (7)$$

where M and $\langle p_T^2 \rangle$ are the multiplicity and average squared transverse momentum for the events, respectively.

The v_1 can be separated into a rapidity-odd component and a rapidity-even component. The rapidity-odd v_1 stems from the deflection of the colliding ions, and hence, changes sign from negative η to positive η . The rapidity-even v_1 is argued to be related to the dipole anisotropy of the pressure gradient arising from the dipole asymmetry of the nuclear overlap; this dipole asymmetry is mainly due to fluctuations in the initial-state geometry.

1. Extraction of dipolar flow (v_1^{even})

For a given centrality selection, the left hand side of Eq. 7 represents the $N \times N$ matrix which we fit with the right hand side using $N + 1$ parameters; N values of $v_1^{even}(p_T)$ and one additional parameter C , the coefficient of momentum conservation. Figs. 15 and 16 illustrates the efficacy of the fitting procedure for central Au+Au collisions at $\sqrt{s_{NN}} =$

200 and 7.7 GeV. The curves in each figure (obtained with Eq. 7) illustrates the effectiveness of the simultaneous fits, as well as the constraining power of the data. That is, $v_{11}(p_T^t)$ evolves from negative to positive values as the selection range for p_T^a is increased.

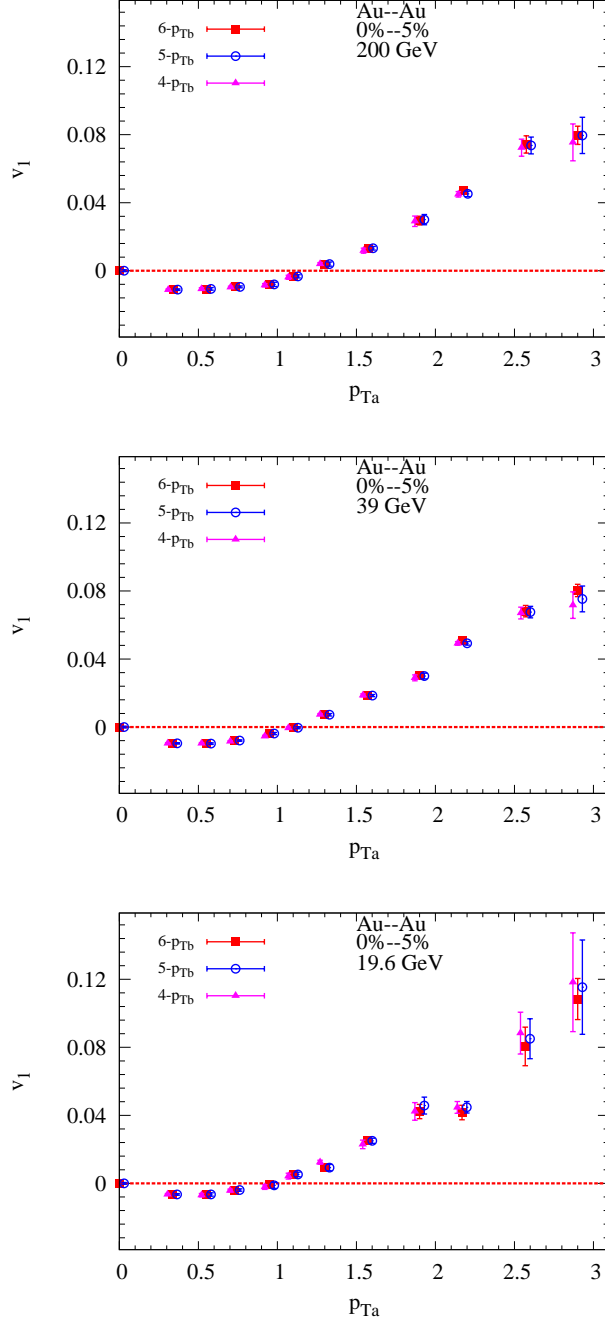


Fig. 17. Extracted v_1 vs. p_T^b for several p_T^a selections. Results are shown for several beam energies as indicated.

Figure 28 shows a representative set of the $v_1^{\text{even}}(p_T)$ values obtained for the beam ener-

gies indicated. In contrast to the rapidity-odd directed flow, these flow values indicate the characteristic pattern of a change from negative $v_1^{even}(p_T)$ at low- p_T , to positive $v_1^{even}(p_T)$ for $p_T \gtrsim 1$ GeV, with a crossing point that shifts with $\sqrt{s_{NN}}$. This predicted pattern for rapidity-even dipolar flow stems from the requirement that the net transverse momentum of the system is zero, *i.e.*, $\langle p_T v_1^{even}(p_T) \rangle = 0$, which implies that the flow direction of low- p_T particles is opposite to that for high- p_T particles. Fig. 18 shows that this requirement is approximately satisfied by the data. It shows that, within specified systematic uncertainties, $\langle p_T v_1^{even}(p_T) \rangle = 0$ for all beam energies. In our subsequent analysis, we imposed the requirement $\langle p_T v_1^{even}(p_T) \rangle = 0$, with an associated systematic uncertainty (see Fig. 18) for the extracted value of $v_1^{even}(p_T)$. This was done to streamline comparisons between the different data sets.

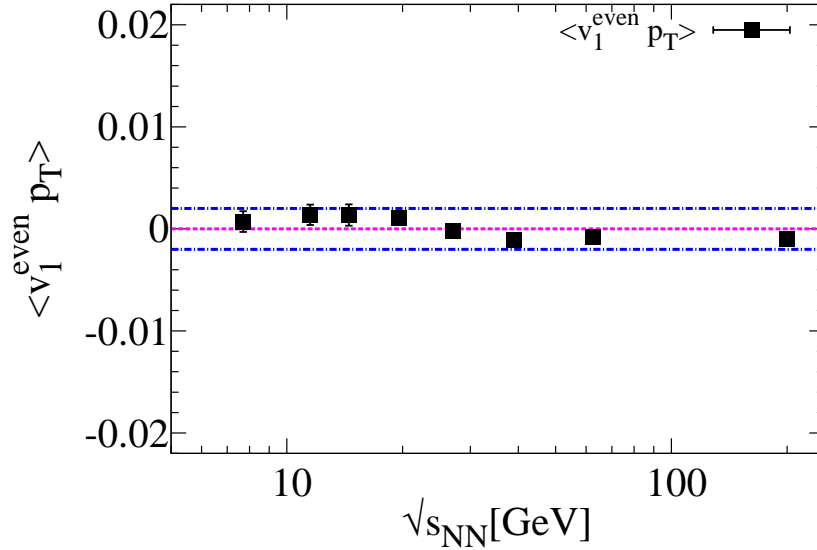


Fig. 18. The beam energy dependence of the net transverse momentum of the system, *i.e.*, $\langle p_T v_1^{even}(p_T) \rangle$ for 0-10% central collisions. The blue dashed lines represent our estimate of the associated systematic uncertainty.

The influence of momentum conservation is different for LS and ULS charged hadrons. Therefore, it is instructive to compare the extracted LS- and ULS- $v_1^{even}(p_T)$ values. Such a comparison is illustrated for a representative centrality selection in Fig. 19. The figure shows that the magnitude and trend for LS- and ULS- $v_1^{even}(p_T)$ are the same within the indicated uncertainties.

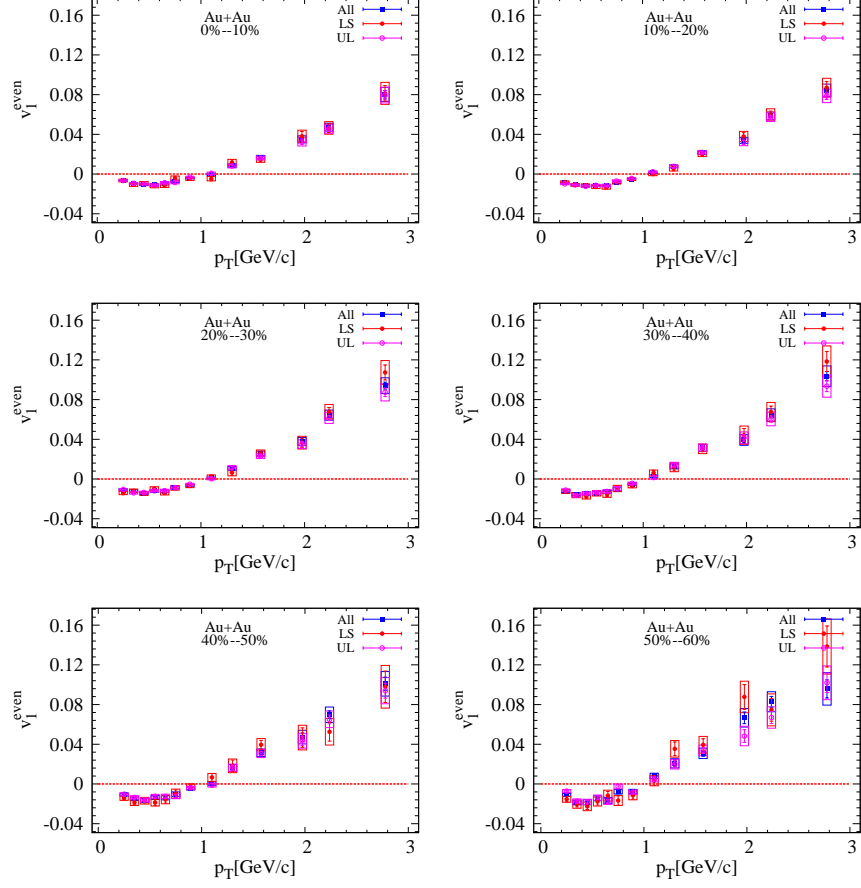


Fig. 19. $v_1^{even}(p_T)$ vs transverse momentum for like and unlike sign selections.

D. Cross-checks

Several cross checks were made for the extracted v_1^{even} data.

- Cross-check with data samples from different years Fig. 20 shows that the results

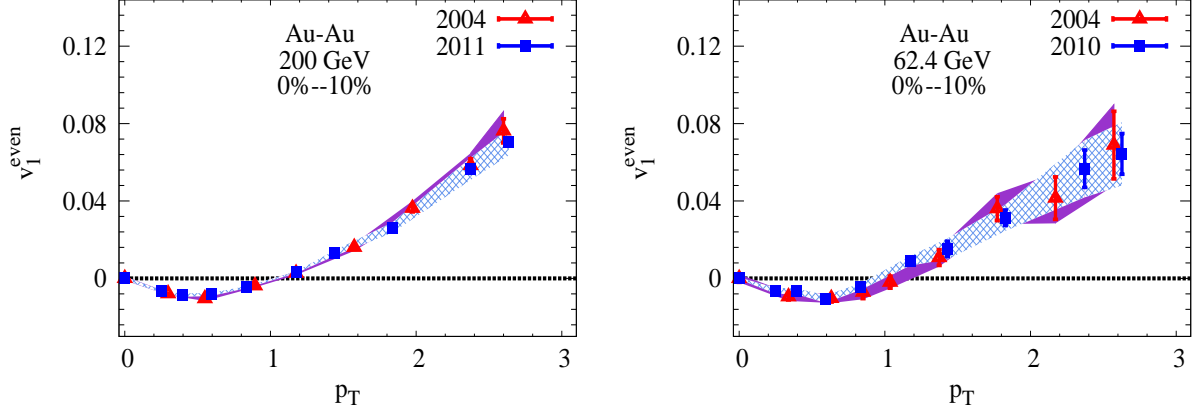


Fig. 20. Illustration of the v_1 Au+Au data ($\sqrt{s_{NN}} = 200$ and 62.6 GeV) for different year.

obtained for the 200 GeV beam energy in different years (2004 and 2011 for 200 GeV and years 2004 and 2010 for 62.4 GeV) are in good agreement.

- Cross-check for different $\Delta\eta$ cuts

Here, we show several comparisons of the v_1^{even} values obtained for different $\Delta\eta$ cuts. Figs. 21 and 22 indicate good agreement between the results for these cuts.

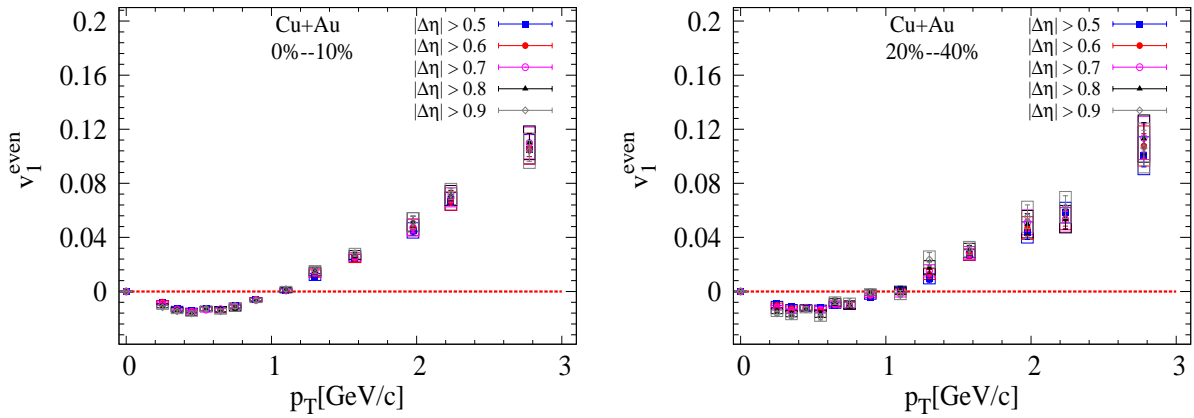


Fig. 21. Illustration of the v_1 for different $\Delta\eta$ cut.

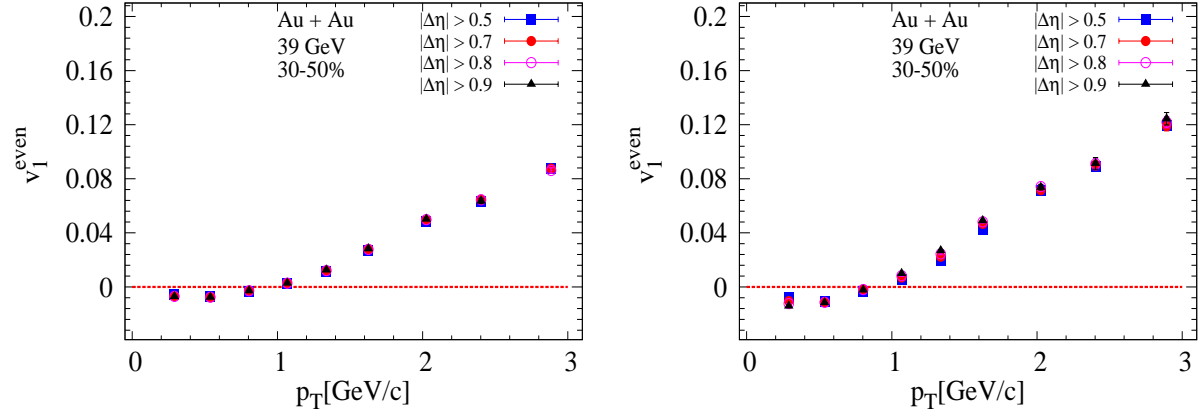


Fig. 22. Illustration of the Au+Au 39-GeV v_1 for different $\Delta\eta$ cut.

E. Systematic uncertainty estimates

There are two primary sources of systematic uncertainties associated with this analysis. Namely, (i) uncertainties associated with construction of the correlation function and the extraction of the v_{11} coefficients, and (ii) uncertainties associated with fitting procedure which enable the extraction of v_1^{even} from v_{11} .

1. Systematic uncertainty estimates associated with the correlation function

In general, these uncertainties are relatively small and stem from (i) the procedure used to suppress short-range non-flow and (ii) uncertainties associated with the acceptance correction for the detector.

- Like-sign vs. un-like sign - see Fig.19

Our study of the influence of a $\Delta\eta$ cut on like-sign vs. unlike-sign charge hadrons indicate a 2% relative uncertainty at higher energy and about 3 – 4% relative uncertainty at low energies, for $|\Delta\eta| > 0.7$.

- p_T^t acceptance corrections - see Fig.23

In this work we use the Mixed-event method which suppresses the effects of detector acceptance. However, we made a cross-check by applying a p_T -dependent efficiency correction following the procedure outlined in the following link (slide 6);

https://drupal.star.bnl.gov/STAR/system/files/BES_v3_AnalysisNote_0.pdf.

This correction did not result in any change to the correlation function as expected - see Fig.23. Also the extracted v_{nn} are shown in Fig.24.

2. Systematic uncertainty estimates associated with the v_{11} fit method

Here, we focus on the checks related to the fitting procedure. For systematic uncertainty estimates, we use the largest and smallest deviations from our study to assign the upper and lower edge of the systematic error bands. It is noteworthy that a similar approach was employed in earlier work summarized in our “Viscous Damping of Anisotropic Flow” analysis note.

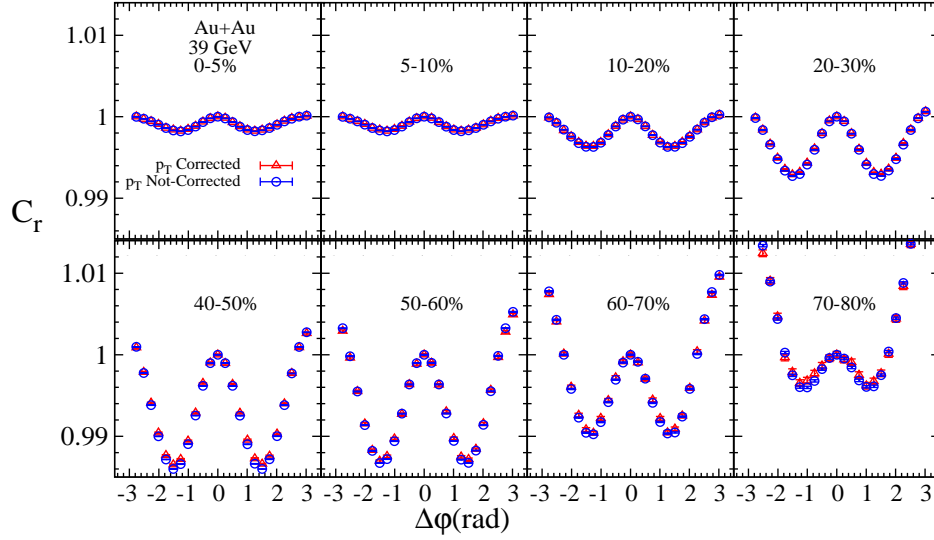


Fig. 23. Illustration of the correlation function for Au+Au data ($\sqrt{s_{NN}} = 39$ GeV) with and without applying the p_T acceptance corrections.

3. Systematic uncertainty from fitting procedure

Figures 15 and 16 show $v_{1,1}(p_T^b, p_T^a)$ for $\sqrt{s_{NN}} = 200$ and 7.7 GeV. The blue dashed lines represent the results of the simultaneous fit. To estimate the systematic uncertainty associated with the fits, we vary the number of p_T^a selections used in the fit to test the fit stability. Figs. 25, 26 and 27 show illustrative examples of $v_{1,1}(p_T^b, p_T^a)$ for 200, 39, 19.6 GeV for 0-5% central events. For each energy, $v_{1,1}(p_T^b, p_T^a)$ is shown for 6, 5 and 4 p_T^a selections respectively. The extracted $v_1(p_T^b)$ for each energy, show relatively small differences with the number of p_T^a values used in the fits, as indicated in Fig. 28.

Figure 28 gives a summary of the overall relative systematic uncertainty as a function of $\sqrt{s_{NN}}$. It shows that the uncertainties are approximately 5% at large values of $\sqrt{s_{NN}}$ but progressively increase to $\sim 20\%$ at the lowest beam energies.

F. Fit χ^2

In tables III and IV we summarize the χ^2/ndf for Fig.(30) and Fig.(31) respectively.

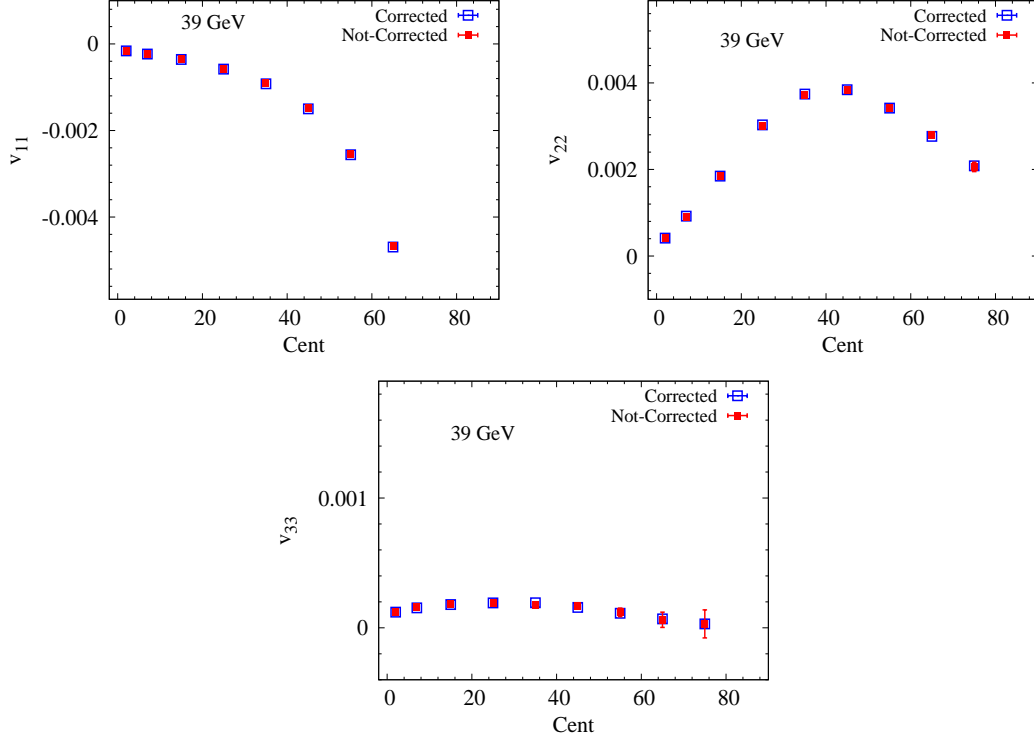


Fig. 24. Comparison for v_{nn} for Au+Au data ($\sqrt{s_{NN}} = 39$ GeV) with and without applying the p_T acceptance corrections.

Fif.(23)	
$\sqrt{s_{NN}}$	Chi^2/ndf
200GeV	1.11
62.4GeV	1.23
39.0GeV	1.28
27.0GeV	1.21
19.6GeV	1.58
14.5GeV	1.24
11.5GeV	1.35
7.70GeV	1.44

Tab. III. Summary of the Chi^2/ndf .

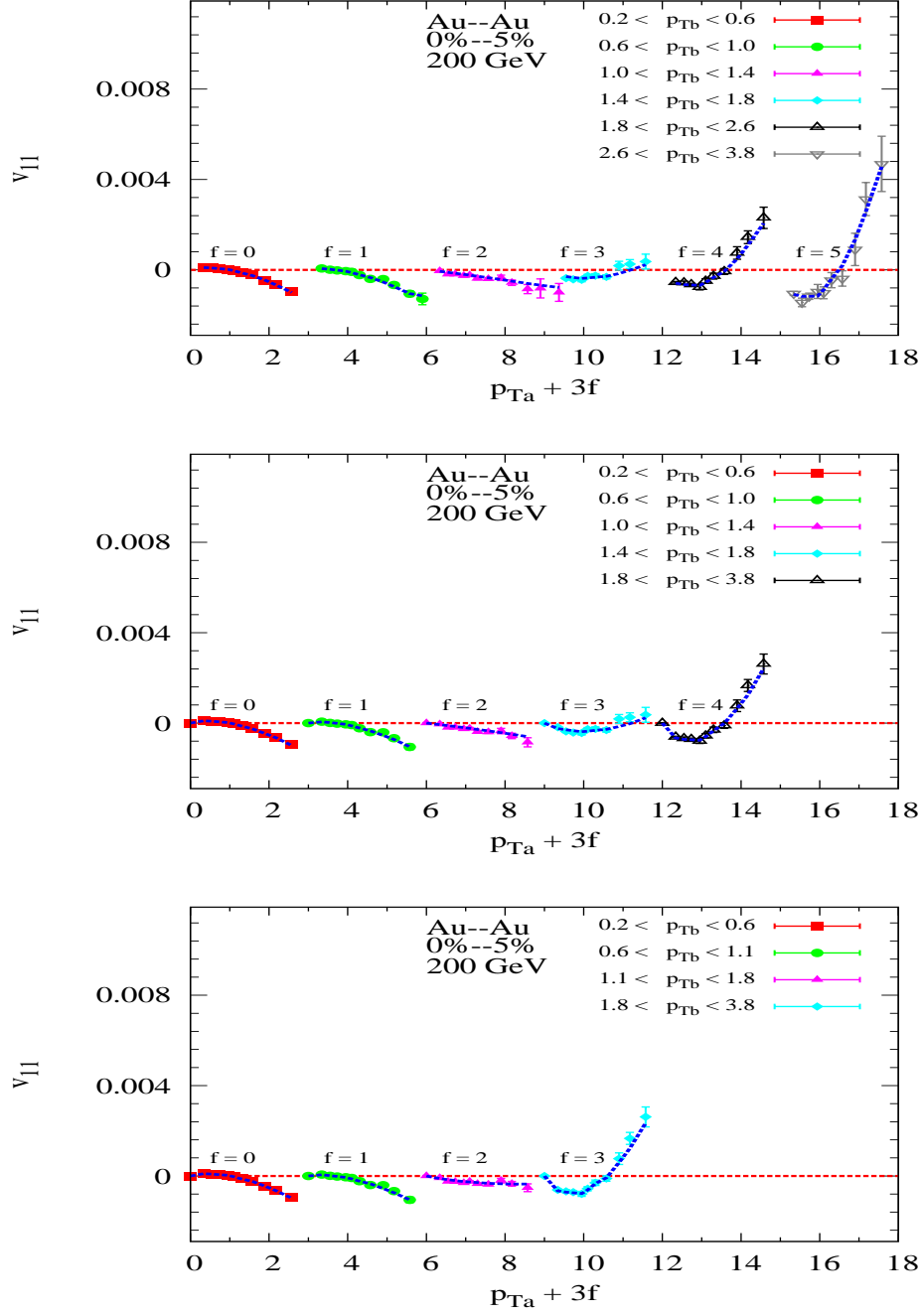


Fig. 25. Illustration of the simultaneous fit of $v_{1,1}$ Au+Au data ($\sqrt{s_{NN}} = 200$ GeV) for different p_T^a with Eq. 7.

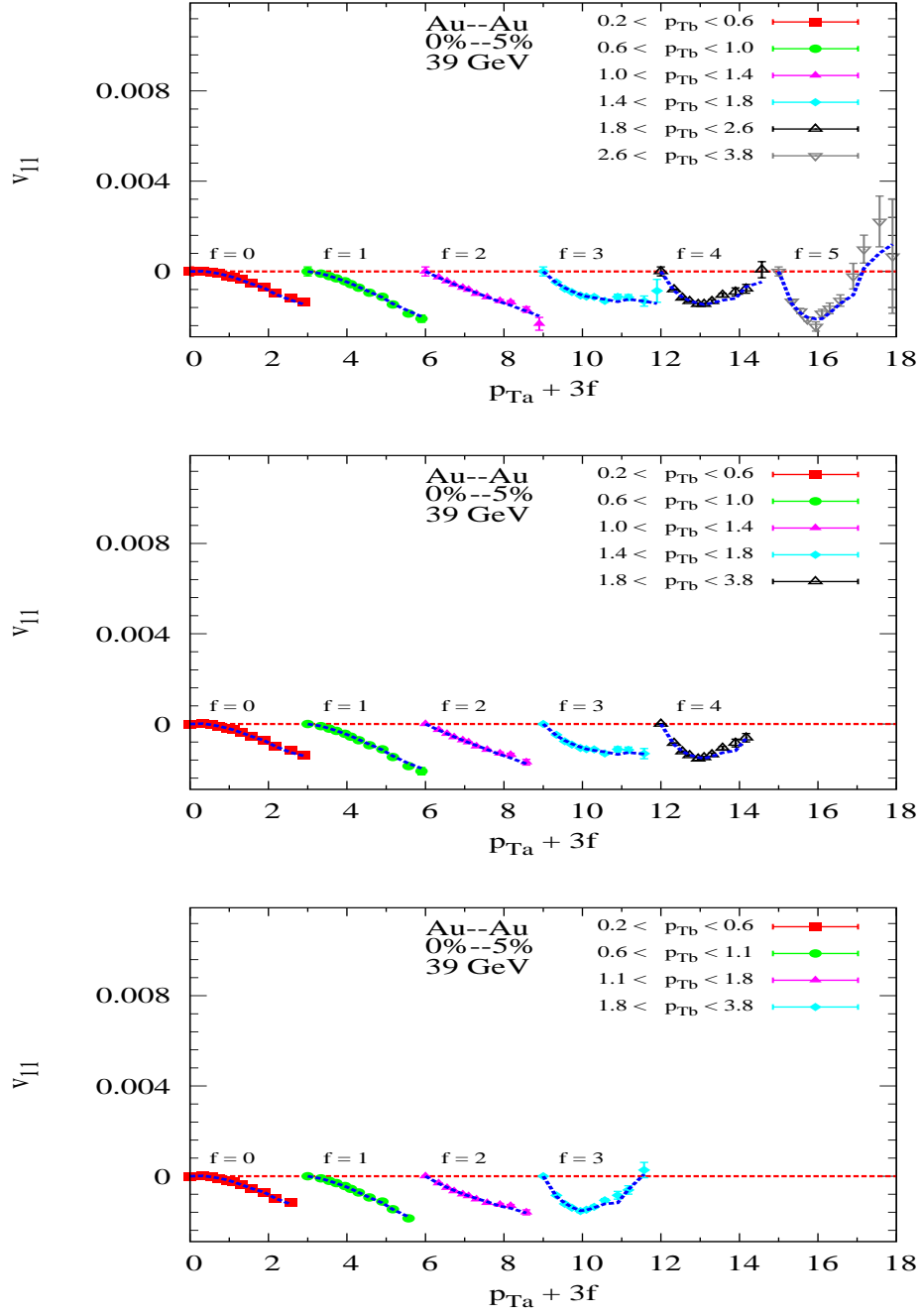


Fig. 26. Illustration of the simultaneous fit of $v_{1,1}$ Au+Au data ($\sqrt{s_{NN}} = 39$ GeV) for different p_T^a with Eq. 7.

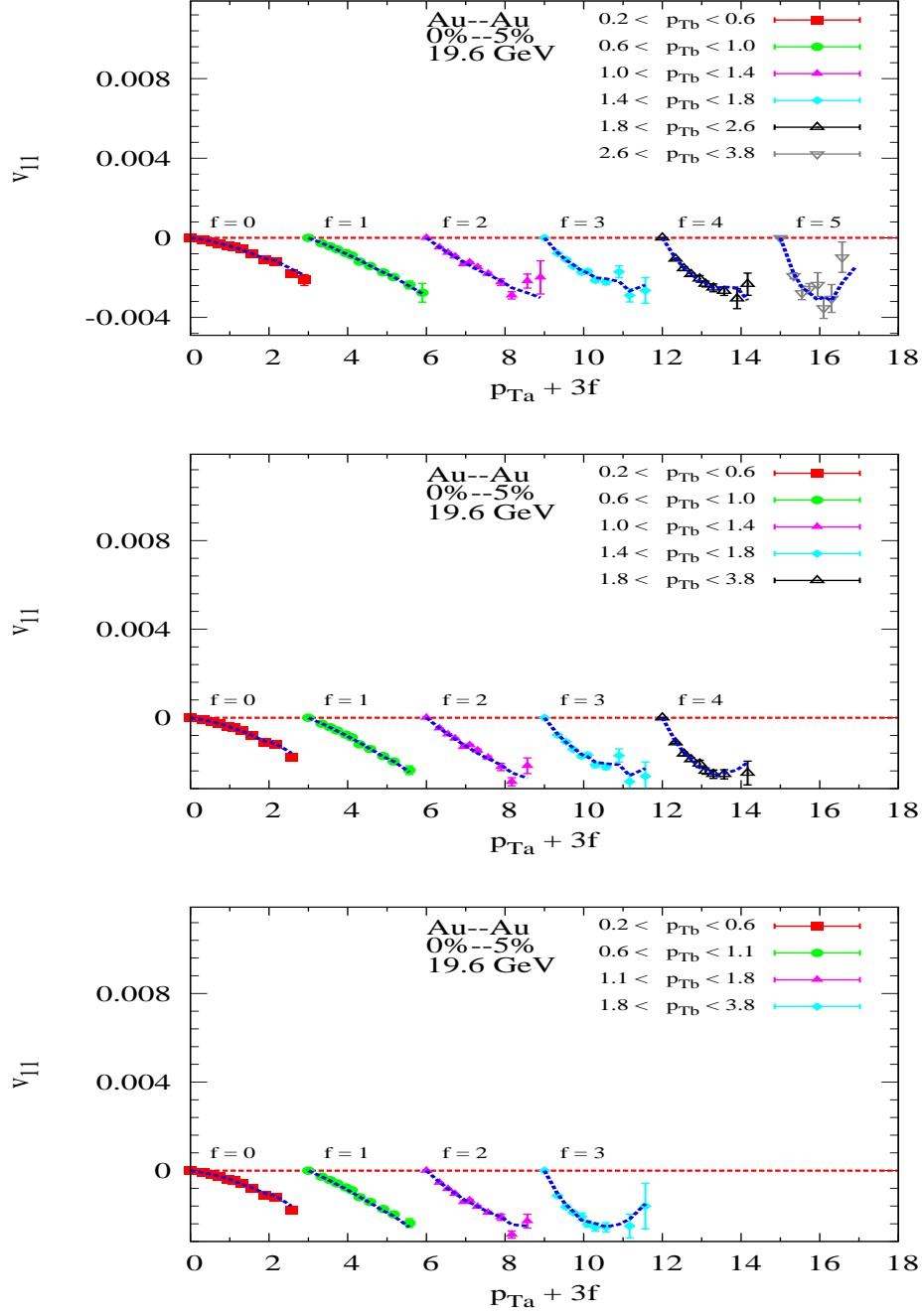


Fig. 27. Illustration of the simultaneous fit of $v_{1,1}$ Au+Au data ($\sqrt{s_{NN}} = 19.6$ GeV) for different p_T^a with Eq. 7.

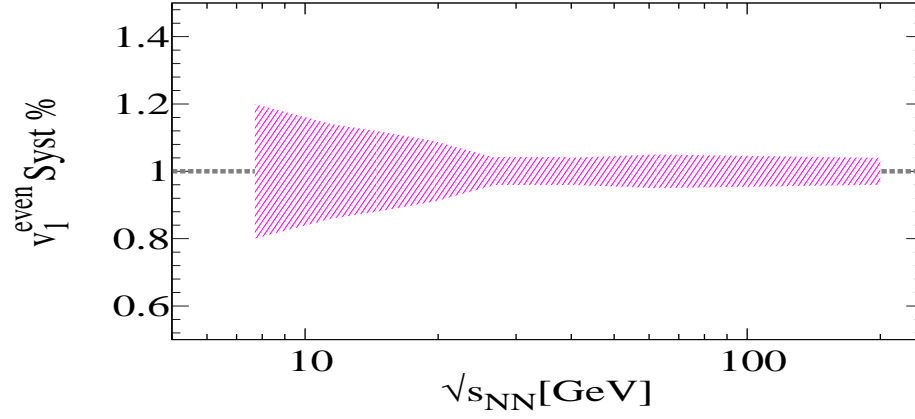


Fig. 28. Illustration of the beam energy dependence of the relative systematic uncertainty for $v_{1,1}$

Fif.(24b)					
200 GeV		39 GeV		19.6 GeV	
<i>Cent</i>	<i>Chi²/ndf</i>	<i>Cent</i>	<i>Chi²/ndf</i>	<i>Cent</i>	<i>Chi²/ndf</i>
5	1.20	5	1.60	5	1.47
10	1.13	10	1.24	10	1.54
20	1.21	20	1.31	20	1.39
30	1.32	30	1.28	30	1.25
40	1.31	40	1.33	45	1.16
50	1.24	50	1.39		
60	1.25	60	1.40		
70	1.44				

Tab. IV. Summary of the Chi^2/ndf .

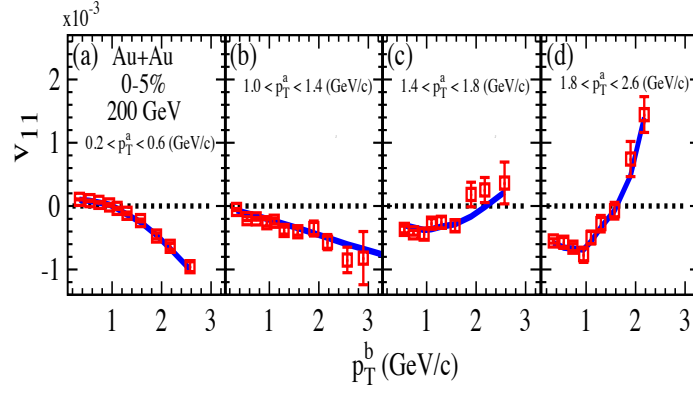


Fig. 29. v_{11} vs. p_T^b for several selections of p_T^a for 0-5% central Au+Au collisions at $\sqrt{s_{NN}} = 200$ GeV. The solid curve shows the result of the simultaneous fit with Eq. 7 (see text).

III. PAPER RESULTS

The proposed figures for the manuscript are Figs.29, 30, 31 and 32.

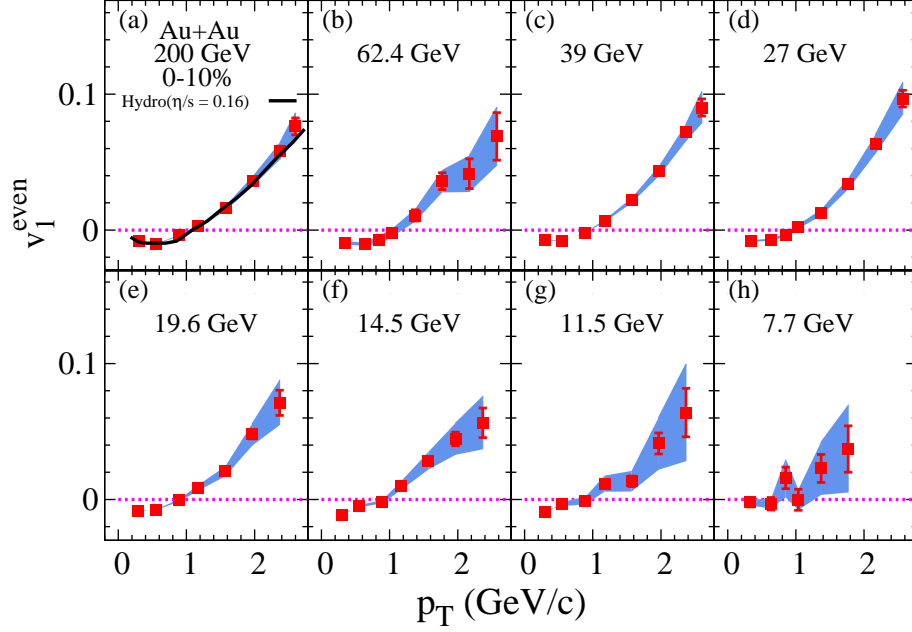


Fig. 30. Extracted values of v_1^{even} vs. p_T for 0-10% central Au+Au collisions for several values of $\sqrt{s_{NN}}$ as indicated; the v_1^{even} values are obtained via fits with Eq. 7; the inset in panel (e) shows a representative set of the associated values of C vs. $\langle \text{Mult} \rangle^{-1}$ (see text). The solid line in panel (a) shows the result from a hydrodynamic calculations. The shaded bands indicate the systematic uncertainties.

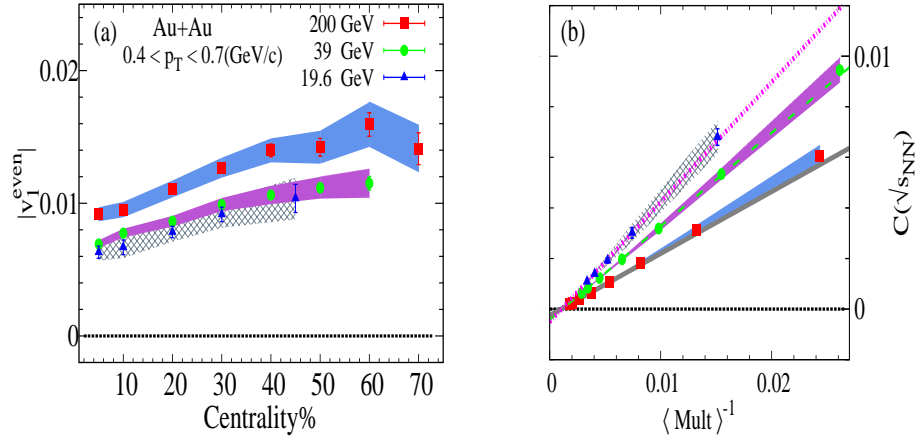


Fig. 31. (a) Centrality dependence of v_1^{even} for $0.4 < p_T < 0.7$ GeV/c for Au+Au collisions at $\sqrt{s_{NN}} = 200, 39$, and 19.6 GeV; (b) C vs. $\langle \text{Mult} \rangle^{-1}$ for the v_1^{even} values shown in (a). The $\langle \text{Mult} \rangle$ values correspond to the centrality intervals indicated in panel (a). The v_1^{even} and C values are obtained via fits with Eq.[6] (see text). The shaded bands indicate the systematic uncertainties.

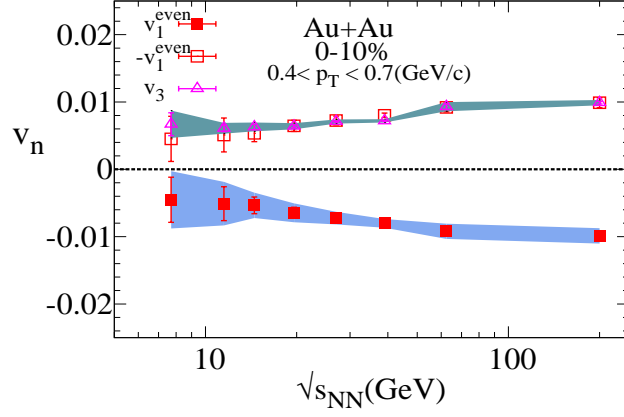


Fig. 32. Comparison of the $\sqrt{s_{NN}}$ dependence of v_1^{even} and v_3 for $0.4 < p_T < 0.7$ GeV/c in 0-10% central Au+Au collisions. The v_1^{even} results are reflected about zero to facilitate a comparison of the magnitudes. The shaded bands indicate the systematic uncertainties.

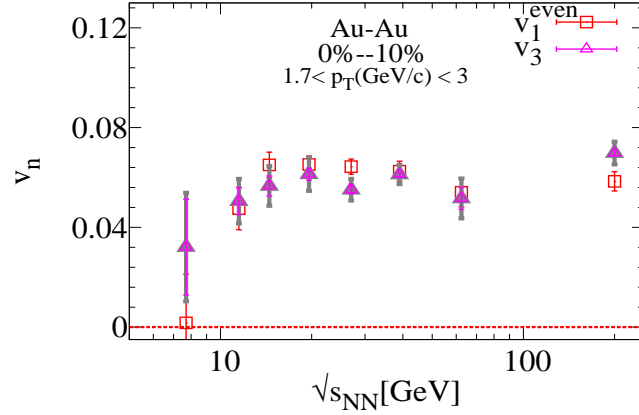


Fig. 33. Comparison of the $\sqrt{s_{NN}}$ dependence of v_1^{even} and v_3 for $1.7 < p_T < 3.0$ GeV/c in 0-10% central Au+Au collisions.
